JGR Atmospheres

RESEARCH ARTICLE
10.1029/2019JD030513

Toward Large-Eddy Simulations of Dust Devils of Observed Intensity: Effects of Grid Spacing, Background Wind, and Surface Heterogeneities

S. Giersch[1], M. Brast[1,2], F. Hoffmann[1,3,4], and S. Raasch[1]

[1]Institute of Meteorology and Climatology, Leibniz University Hannover, Hannover, Germany, [2]Now at METEK Meteorologische Messtechnik GmbH, Elmshorn, Germany, [3]Now at Cooperative Institute for Research in Environmental Sciences (CIRES), University of Colorado Boulder, Boulder, CO, USA, [4]Now at Chemical Sciences Division, NOAA Earth System Research Laboratory (ESRL), Boulder, CO, USA

Key Points:
- First numerical simulations producing dust devil-like vortices of observed intensity are presented
- Grid spacings of 2 m, heating heterogeneities, and moderate background winds increase the strength of simulated dust devils significantly
- Over heterogeneous surfaces, dust devil-like vortices cumulate at low-level convergence lines

Correspondence to:
S. Raasch,
raasch@muk.uni-hannover.de

Citation:
Giersch, S., Brast, M., Hoffmann, F., & Raasch, S. (2019). Toward large-eddy simulations of dust devils of observed intensity: Effects of grid spacing, background wind, and surface heterogeneities. *Journal of Geophysical Research: Atmospheres*, *124*, 7697–7718. https://doi.org/10.1029/2019JD030513

Received 19 MAR 2019
Accepted 23 MAY 2019
Accepted article online 8 JUL 2019
Published online 29 JUL 2019

Author Contributions

Conceptualization: S. Giersch, F. Hoffmann, S. Raasch
Data curation: S. Giersch
Methodology: S. Giersch, M. Brast, F. Hoffmann, S. Raasch
Software: S. Giersch, M. Brast, F. Hoffmann
Validation: S. Giersch
Writing - Original Draft: S. Giersch, F. Hoffmann
Formal Analysis: S. Giersch, F. Hoffmann
Investigation: S. Giersch, F. Hoffmann
Project Administration: S. Raasch
Resources: M. Brast, F. Hoffmann

Abstract Dust devils are convective vortices with a vertical axis of rotation made visible by lifted soil particles. Currently, there is great uncertainty about the extent to which dust devils contribute to the atmospheric aerosol input and thereby influence Earth's radiation budget. Past efforts to quantify the aerosol transport and study their formation, maintenance, and statistics using large-eddy simulation (LES) have been of limited success. Therefore, some important features of dust devil-like vortices simulated with LES still do not compare well with those of observed ones. One major difference is the simulated value of the core pressure drop, which is almost 1 order of magnitude smaller compared to the observed range of 250 to 450 Pa. However, most of the existing numerical simulations are based on highly idealized setups and coarse grid spacings. In this study, we investigate the effects of various factors on the simulated vortex strength with high-resolution LES. For the fist time, we are able to reproduce observed core pressures by using a high spatial resolution of 2 m, a model setup with moderate background wind and a spatially heterogeneous surface heat flux. It is found that vortices mainly appear at the lines of horizontal flow convergence above the centers of the strongly heated patches, which is in contrast to some older observations in which vortices seemed to be created along the patch edges.

1. Introduction

Dust devils are convective vortices with a vertical axis and the capability to lift dust. This capability makes dust devils not only an interesting optical phenomenon but also an important part of the climate system: Dust devils are known to increase the transport of dust from the surface to the atmosphere by several orders of magnitude compared to their background values of the dust flux (Renno et al., 2004). Therefore, dust devils have to be considered in the global dust budget with commensurate influences on cloud formation processes, the global radiation budget, or the water and carbon cycle (Shao et al., 2011). However, the contribution that dust devils have to the global dust budget is still under debate (e.g., Jemmett-Smith et al., 2015; Koch & Renno, 2005). To quantify the different effects of the aerosol transport through dust devils into the atmosphere, sufficient statistics on the occurrence and strength of dust devils are required. But the derivation of these statistics is rather difficult. First, observations suffer from the erratic occurrence of dust devils and the limited area, which can be reliably monitored (e.g., Lorenz, 2014). Second, numerical simulations, from which the deviation of these statistics would be straightforward, have not been able to reproduce dust devils of observed intensities (e.g., Kanak, 2006). In particular, the highest simulated core pressure drop of 72.4 Pa (Raasch & Franke, 2011) is still almost 1 order of magnitude smaller than typically observed values in the range of 250 to 450 Pa (Sinclair, 1973; Kanak, 2005, 2006). Thus, the main objective of this study is the identification of reasons for this deviation of numerical simulations from observations and, consequently, the simulation of dust devils of observed intensity.

Large-eddy simulation (LES) models are the most common method for simulating the development of dust devils in the convective boundary layer (CBL; e.g., Gheynani & Taylor, 2010; Kanak, 2005; Kanak et al., 2000; Ito et al., 2013; Raasch & Franke, 2011). For this task, the simulations have to fulfill two demands. First, they have to simulate a domain sufficiently large enough to represent the cellular pattern of convection,

Supervision: S. Raasch
Visualization: S. Giersch, F. Hoffmann
Writing - review & editing: S. Giersch, M. Brast, F. Hoffmann, S. Raasch

whose vertices are believed to be necessary for the generation of dust devils (e.g., Kanak, 2005; Raasch & Franke, 2011). And second, they have to resolve dust devils themselves by a sufficiently fine resolution. To cover both needs, a model domain of a couple of kilometers in each horizontal direction and a grid spacing in the order of tens of meters or less are necessary. In this way, however, a dust devil is resolved by a couple of grid points only. Structures on these scales are just partly resolved (e.g., Sagaut, 2006, Chapter 7), giving a possible explanation for the deviation between simulations and observations. Accordingly, this study will analyze how the grid spacing affects the intensity of simulated dust devils first.

Furthermore, the effect of the simulated environment in which the dust devils will develop is investigated. In past dust devil simulations, setups have been highly idealized, neglecting background winds and heterogeneous surface heating (e.g., Kanak et al., 2000; Ohno & Takemi, 2010). In fact, these are conditions rarely found in nature, and previous studies show that these parameters may affect the occurrence and strength of dust devils significantly. For instance, LES of Raasch and Franke (2011) showed that moderate background winds enhance and intensify the formation of dust devil-like vortices, whereas strong background winds decrease their occurrence in accordance with observations (Sinclair, 1969). Moreover, Sinclair (1969) and Renno et al. (2004) observed that heterogeneous surfaces, caused by different patterns of heating or surface roughness, affect the formation of dust devils, too. Rugged terrain, such as mountains, prevents dust devils from developing, while heterogeneous conditions, such as hills or dry riverbeds, can be favorable. Both effects, background winds and the pattern of surface heating, will be studied in the following.

All in all, this study will offer an overview of several factors affecting the strength of simulated dust devils, aiming the first simulation of dust devils of observed intensity. In addition, the first LES especially designed for investigating the impact of heterogeneities on the intensity of dust devils is introduced. In the following, the term dust devil refers to all convective vortices exceeding certain core pressure drop and vorticity thresholds (section 2.2). Furthermore, vortex, dust devil, and dust devil-like vortex are used as synonyms. The paper is structured as follows. The applied simulation setups and analysis methods are described in section 2. The results are presented in section 3. A summary concludes this study in section 4.

2. Methodology

All simulations are carried out with the Parallelized Large-Eddy Simulation Model (PALM; Maronga et al., 2015), which solves the nonhydrostatic, filtered, incompressible Navier-Stokes equations in Boussinesq-approximated form and an additional transport equation for potential temperature. Time stepping is based on a third-order Runge-Kutta scheme (Williamson, 1980); advection is approximated by a fifth-order scheme by Wicker and Skamarock (2002). In addition, subgrid-scale mixing is parameterized based on a 1.5th-order closure after Deardorff (1980). PALM uses the modified version of Moeng and Wyngaard (1988) and Saiki et al. (2000).

The application of the Boussinesq-approximation requires incompressibility of the flow, which is not satisfied by the numerical integration of the governing equation used in PALM. Hence, a predictor-corrector method (Patrinos & Kistler, 1977) is used, in which a Poisson equation for the so-called perturbation pressure is solved, guaranteeing the incompressibility of the flow. In case of horizontally homogeneous heating the absolute value of the perturbation pressure is interpreted as the pressure drop within dust devils as it is done similarly in studies of, for example, Kanak et al. (2000), Kanak (2005), and Raasch and Franke (2011). However, for the simulations with heterogeneous heating, where mean pressure gradients along the heterogeneity arise (see section 3.4), a different interpretation of the perturbation pressure is required. Instead of absolute values, relative values of the perturbation pressure with respect to the instantaneous average along the homogeneous direction are interpreted as the pressure drop (see section 2.2 for a more detailed explanation).

Due to their inherent errors, the application of a suitable advection scheme is mandatory to allow a sufficient development of small-scale phenomena like dust devils, covering only a couple of grid points. Usually, schemes of odd order of accuracy are dominated by numerical diffusion, damping small-scale features of the flow. Numerical dispersion is predominantly occurring for schemes of even order. It provokes instabilities (also known as wiggles) in the vicinity of strong gradients (Hirsch, 2007, Chapter 8; Durran, 2010, Chapter 3), being inherent features of dust devil centers. Therefore, an artificial increase of the collapse of dust devils through numerical dispersion has been observed in our simulations if a second-order advection scheme by Piacsek and Williams (1970) is used (not shown). To avoid this, high-order and less dispersive advec-

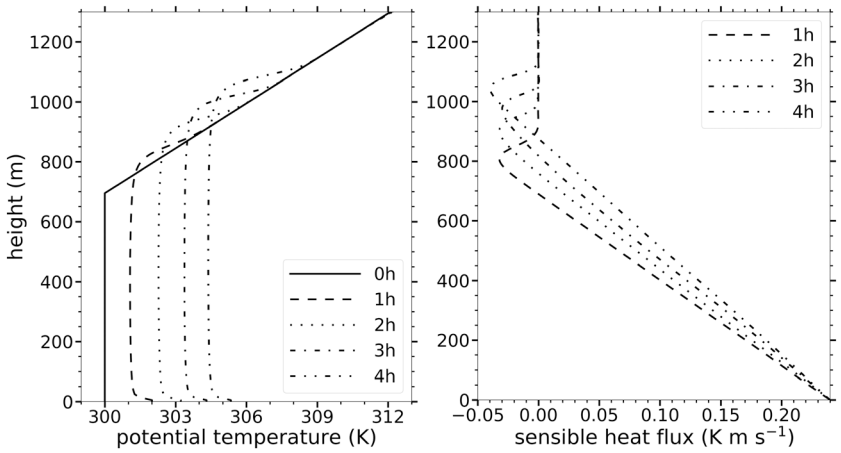

Figure 1. Horizontally and temporally averaged profiles of the potential temperature (left) and sensible heat flux (right) for four different simulation times derived from HO. The initial profile of the potential temperature is indicated by the solid line.

tion schemes are necessary, like the fifth-order scheme by Wicker and Skamarock (2002). It is based on an approximation of the advection term of even accuracy (viz., sixth order), which causes numerical dispersion. Due to the addition of an artificial dissipation term, the order of the scheme is reduced by one and the wiggles produced by the dispersion error are damped by numerical diffusion. Thus, a better representation of vortices and the associated strong gradients can be reached in comparison to the second-order scheme by Piacsek and Williams (1970), used in an earlier LES study on dust devils by Raasch and Franke (2011).

2.1. General Setup

For this study, several different simulations of a dry atmospheric boundary layer have been conducted. This subsection will give an overview of their initialization. In all simulations with homogeneous heating, a CBL is simulated by prescribing a constant sensible surface heat flux of 0.24 K·m·s^{-1} (approximately 285 W/m^2), which is a typical value for clear-sky situations in the middle latitudes during the afternoon in spring and summer (e.g., Cellier et al., 1996; Parlow, 2003). For the heterogeneous simulation, this heat flux is split in two equally sized rectangles of 0.12 K·m·s^{-1} (140 W/m^2) and 0.36 K·m·s^{-1} (430 W/m^2), resulting in a domain-averaged flux of 0.24 K·m·s^{-1} (285 W/m^2) as applied in the homogeneous simulations. An idealized profile of potential temperature is specified at the beginning of the simulation featuring a constant value of 300 K up to 700 m followed by a capping inversion of 0.02 K/m (see Figure 1). Well above the capping inversion a sponge layer is applied, where Rayleigh damping reduces spurious reflections of vertically propagating waves. The horizontal wind components are initialized by using a height-constant geostrophic wind, being a synonym for the background wind in the following. To trigger off the onset of convection, random perturbations are imposed on the horizontal velocity field at the beginning of the simulation.

At the bottom boundary, a no-slip condition is prescribed for the horizontal wind components. A free-slip condition is used at the top boundary. In addition, doubly periodic boundary conditions are used. For calculating the momentum flux at the surface, a constant flux layer is assumed as the boundary condition between the surface and the first grid level, using Monin-Obukhov similarity theory. This requires a value for the roughness length, which is set to 0.1 m (typical for rural areas). The Coriolis parameter is set to 1.26×10^{-4} s^{-1} corresponding to a latitude of 52°.

A quadratic model domain of 4×4 km^2 is applied in the horizontal directions to resolve the pattern of convective cells adequately. As stated in section 1, this is necessary since the vertices of these cells are the primary source for the formation of dust devils and have to be resolved for a successful simulation of dust devils (e.g., Kanak, 2005; Raasch & Franke, 2011). The height of the model domain is located well above the inversion (1,900–2,100 m) to not interact with the growing CBL. Above 1,200 m, the vertical grid spacing is stretched. Very high resolution LES of 2-m grid spacing are carried out for selected simulations. Most simulations, however, are conducted with a (still relatively high) resolution of 10 m as a compromise between resolution and computing costs. The simulated time is restricted to 14,400 s. This is a further compromise between compu-

Table 1
Summary of Characteristics of the Conducted Simulations

Simulation name	Domain size $L_x \times L_y \times L_z$ (m^3)	Number of grid points	Grid spacing (m)	Wind speed (m/s)	Wind direction	Heterogeneity (width in kilometers)
HO	4,000 × 4,000 × 1,950	400 × 400 × 144	10	0	—	no
HOhf	4,000 × 4,000 × 1,950	400 × 400 × 144	10	0	—	no
HOhr	4,000 × 4,000 × 1,782	2,000 × 2,000 × 640	2	0	—	no
HOu2.5	4,000 × 4,000 × 1,950	400 × 400 × 144	10	2.5	*x*	no
HOu5	4,000 × 4,000 × 1,950	400 × 400 × 144	10	5	*x*	no
HOu7.5	4,000 × 4,000 × 1,950	400 × 400 × 144	10	7.5	*x*	no
HOu10	4,000 × 4,000 × 1,950	400 × 400 × 144	10	10	*x*	no
HE	4,000 × 4,000 × 1,950	400 × 400 × 144	10	0	—	yes (4)
HE2	4,000 × 4,000 × 1,950	400 × 400 × 144	10	0	—	yes (2)
HE8	8,000 × 4,000 × 1,950	800 × 400 × 144	10	0	—	yes (8)
HE16	16,000 × 4,000 × 1,950	1,600 × 400 × 144	10	0	—	yes (16)
HEv5	4,000 × 4,000 × 1,950	400 × 400 × 144	10	2.5	*y*	yes (4)
HEv5hr	4,000 × 4,000 × 1,782	2,000 × 2000 × 640	2	5	*y*	yes (4)

Note. HE = heterogeneous; HO = homogeneous.

tational costs and providing sufficient dust devil statistics that heavily depends on the resolution, domain size, and simulated time.

An overview of all conducted simulations is given in Table 1, stating varied parameters: domain size, number of grid points, grid spacing, wind speed, wind direction, and pattern of heating (homogeneous/heterogeneous with different widths of the heterogeneity). Moreover, the table assigns a name to each simulation, which will be used as a reference in the following. The first part of the name indicates homogeneous ("HO") or heterogeneous ("HE") simulations. Then, if a background wind is imposed, the wind direction ("*u*" / "*v*" for the wind in *x* or *y* directions, respectively) and the absolute value of the wind speed (m/s) are given. If applicable, special characteristics of the simulation like an increased heat flux, different widths of the heterogeneity, or the resolution are indicated at the end of the name: "hr" stands for "high-resolution simulation" with a grid spacing of 2 m, "hf' stands for "high heat flux" with a sensible heat flux of 0.36 $K \cdot m \cdot s^{-1}$.

2.2. Vortex Detection and Analysis

For vortex detection, the same algorithm as developed and used by Raasch and Franke (2011) is applied. This subsection will briefly summarize this algorithm and mention changes and additions that have been necessary for this study. The reader is referred to Raasch and Franke (2011) for a more detailed description.

Vortices are detected at the first computational grid point above the surface by identifying local maxima (or relative maxima in case of heterogeneous simulations) of the absolute value of perturbation pressure drop $|p|$ and the absolute value of vorticity, which describes the vertical component of rotation of the velocity field

$$|\zeta| = \left| \frac{\partial v}{\partial x} - \frac{\partial u}{\partial y} \right|, \tag{1}$$

where u and v are the horizontal velocity components in x and y directions, respectively. For simulations with heterogeneous heating (see section 3.4), values of the perturbation pressure drop relative to the instantaneous average along y (homogeneous direction) are considered. This is due to the fact that with heterogeneous heating along x a secondary circulation parallel to the x axis develops, which is caused by a large-scale negative perturbation pressure drop over the stronger heated area and positive perturbation pressure drop over the less heated region. Thus, the mean reference perturbation pressure is not 0 anymore. Typical values for the mean reference perturbation pressure are several pascals (e.g., Letzel & Raasch, 2003).

For all simulations with a grid spacing of 10 m, a dust devil-like vortex is identified if $|\zeta| \geq 0.087\,s^{-1}$ and $|p| \geq 3.5$ Pa, which would correspond to a tangential velocity at the dust devil's wall of 1.7 m/s and a wall radius of 20 m (according to the Rankine vortex model, where the vortex wall corresponds with the maximum tangential velocity). At the same time, the pressure minimum needs to be located at the maximum of

the vorticity or at an adjacent grid point. This takes into account that the location of the pressure minimum and the axis of rotation can be slightly different. The applied thresholds correspond to 5 times the standard deviation of vorticity and 3 times the standard deviation of perturbation pressure. The standard deviation is calculated from HO (or HOhr for the high-resolution LES) using an instantaneous horizontal cross section taken from the analysis height after 4 hr of simulation time. This procedure is in good agreement with other dust devil detection algorithms (e.g., Nishizawa et al., 2016).

The used thresholds for detecting dust devils seems to be quite low compared to observational data. For example, a pressure value of at least 30 Pa is necessary to lift dust under ideal conditions (Lorenz, 2014). Low values, however, are necessary to record almost the entire life cycle of the vortex. Nevertheless, the very initial and very last phase of a dust devil's life cannot be recorded. The selection of the thresholds is also a compromise between getting a sufficiently large amount of data for analysis and eliminating the random noise of noncoherent turbulence as much as possible. Since the high-resolution LES (2-m grid spacing) tend to produce dust devils of higher intensity, the threshold values are $|\zeta| \geq 0.32\,\mathrm{s}^{-1}$ (5 times the standard deviation) and $|p| \geq 3.5$ Pa (3 times the standard deviation) for these runs. The different thresholds for different grid spacings do not affect the comparability of the simulations since we are mainly interested in intense dust devils, which feature most of the time much higher values than the applied threshold values.

For dust devil track analysis, the vortex center identified at a certain model time step is connected to a vortex center at the following time step (or the time step after that) if the distance between both is less or equal than two grid points. Allowing the vortex to be not detected at the following (first) time step but at the time step thereafter (second time step) takes into account that the vorticity or the perturbation pressure could be momentarily just less than the threshold value. An additional criterion to avoid counting two different dust devil centers to the same track is that the vorticity have to have the same sign at any time step of the track. Sometimes several dust devil centers are detected in the vicinity of each other during one specific time step. This might be the case for dust devils deviating strongly from a circular pattern resulting in several local extrema that are erroneously identified as dust devil centers (or for the rare case of a dust devil consisting of several vortices, which have also been observed in nature; Bluestein et al., 2004). To avoid counting a single dust devil twice or more, the weaker vortex centers (rated by the core pressure drop) located within the dust devils radius are rejected before track analysis. The vortex radius is determined from the tangentially averaged pressure drop distribution around each center. The distance where the pressure drop is reduced to 50% of the core pressure drop is assumed to be the radius of the vortex. This radius criterion matches most of the common vortex models, which try to define the dust devil structure analytically (e.g., Lorenz, 2014).

3. Results

Before advancing to the analysis of several parameters affecting the intensity of simulated dust devils, the following subsection will give a general overview of the control simulation HO. Afterward, we will modify HO's setup systematically to test the effect of grid spacing, background wind, and heterogeneities to work out their individual impacts on the intensity of simulated dust devils.

3.1. Control Simulation HO

The general development of the CBL in HO can be generalized to all following simulations. Figure 1 displays horizontally and temporally averaged vertical profiles of the potential temperature and the vertical sensible heat flux at several points in time. In this study, time averaging will always refer to a period of 900 s before the respective output time. The profiles indicate a well-mixed boundary layer growing in time. Due to the heating from the surface, the lowest meters feature an unstable stratification, which is a necessary condition for the development of dust devils (e.g., Sinclair, 1969). The vertical profiles of the sensible heat flux exhibit the prescribed value of $0.24\,\mathrm{K{\cdot}m{\cdot}s}^{-1}$ at the surface, which decreases monotonically throughout the boundary layer, indicating that the simulation has reached a quasi-stationary state after 1 hr. Earlier times (<2,700 s) are considered as model spin-up and not analyzed.

The cellular pattern of the simulated CBL is visible in horizontal cross sections of the vertical velocity at different heights after 10,800-s simulated time (Figure 2). The cells are dominated by high positive velocities at the cell edges, whereas negative velocities cover the cell centers. For the applied horizontal domain size of $4\times4\,\mathrm{km}^2$, about two to three dominant cells in each horizontal direction are represented (Figure 2, bottom). Above one third of the boundary layer height, the polygonal structure changes to a pattern consisting of

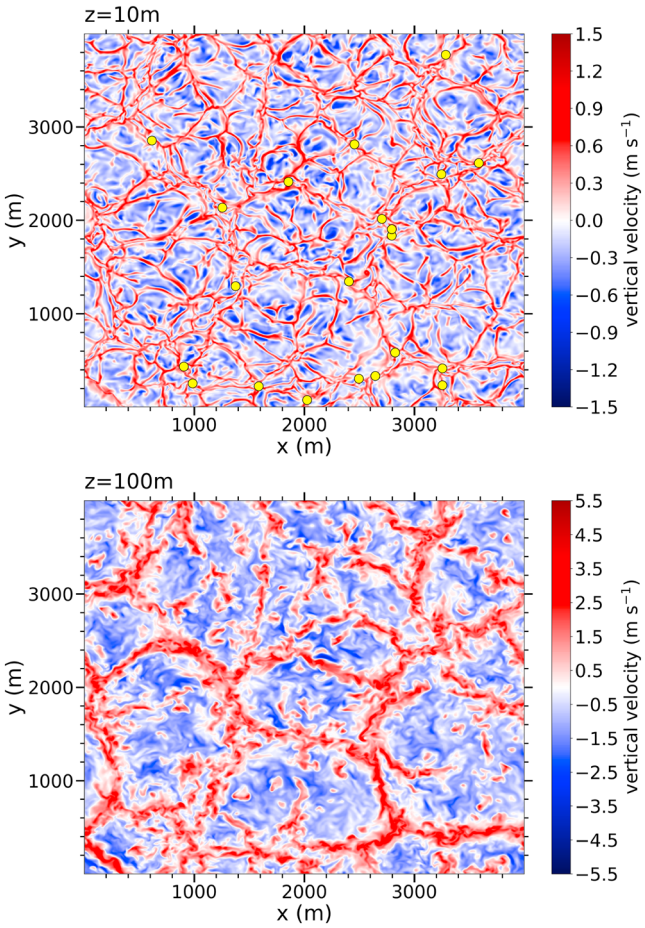

Figure 2. Horizontal cross sections of the instantaneous vertical velocity at 10 m (top) and 100 m (bottom) height after 10,800-s simulated time derived from simulation HO. Detected vortex centers are depicted as yellow dots.

several isolated plumes with strong updrafts and widespread downdrafts (not shown), which is a well-known behavior of the CBL (e.g., Schmidt & Schumann, 1989).

At 10-m height, the vertical velocity exhibits a finer cellular pattern than at higher levels. However, the locations of vortex centers (yellow dots) coincide well with the cell vertices where, due to the horizontal convergence, higher vertical velocities arise than in the cell centers and several convergence lines merge. This finding is in accordance with previous studies (e.g., Kanak, 2005; Raasch & Franke, 2011), which have elaborated that the cell edges and especially the vertices are the primary location of dust devil generation.

The significant contribution of cell vertices to the development of vertical vortices is also confirmed by the spatial distribution of dust devil tracks detected between 9,000 and 14,400 s (Figure 3): The tracks clearly resemble the pattern of convective cells due to their preferential occurrence at the cell vertices and edges. Overall, 1,952 vortex tracks were detected during this 1.5-hr period.

To further analyze how statistics change between the different simulations, some bulk characteristics are compiled in Table 2, which lists, from left to right, the number of detected dust devils N, averaged lifetime $\bar{\tau}$, translation or migration speed $\overline{v_{t_{mean}}}$, radius $\overline{r_{mean}}$, maximum core pressure drop $\overline{|p|_{max}}$, maximum vorticity $\overline{|\zeta|_{max}}$, and maximum tangential velocity $\overline{\langle u_{tan}\rangle_{max}}$. The overbar describes an average over all N detected vortices, whereas the angle brackets refer to the maximum of a tangentially averaged value determined for each dust devil center. The index "max" refers to the maximum value during the whole lifetime of one specific vortex, and the index "mean" indicates a value averaged over the whole lifetime of a single vortex. Besides, the standard deviations and the overall maximum values are shown in Table 2. For all the following

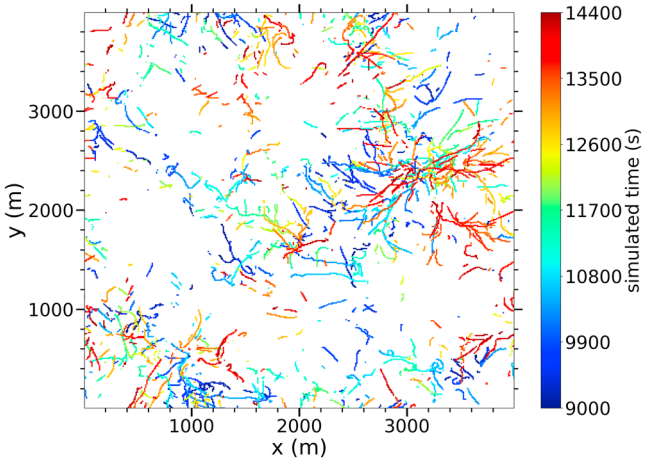

Figure 3. Spatial distribution of all 1,952 vortex tracks between 9,000 and 14,400 s derived from simulation HO. Each vortex center is represented by a dot. The color of the dot codes the simulated time at detection.

statistics, only vortices after the model spin-up (>2,700 s) with a lifetime of

$$\tau > \max\left(120\,\mathrm{s}, \frac{2\pi r_{\mathrm{mean}}}{\langle u_{\tan}\rangle_{\mathrm{mean}}}\right) \tag{2}$$

are considered. Equation (2) says that a vortex has to exist for at least 120 s and that an air parcel flowing with $\langle u_{\tan}\rangle_{\mathrm{mean}}$ can circulate the vortex once or more during its lifetime. This procedure restricts the statistics to the longer-lasting and thereby stronger dust devil-like vortices, which are much more relevant in the discussion of simulating realistic maximum core pressure drops. Nevertheless, for the presentation of the spatial distribution of dust devil-like vortices (e.g., Figure 3) each vortex track independent of its lifetime is considered.

It should be mentioned here that the main reason for listing bulk properties is to afford others a better comparison of their model results with this study. However, the focus of discussion and analysis is on the maximum core pressure drop. For the mean value of this parameter, the confidence interval with a confidence level of 95% is specified for each simulation in order to account for statistical significance. Simulation HO shows a confidence interval of [8.71 Pa, 9.30 Pa]. In addition, no linear correlation could be found between vortex radius and core pressure drop as well as between the vortex radius and its duration for each of the following simulations. This is indicated by Pearson correlation coefficients, which are around 0.2 or lower.

3.2. The Effect of Grid Spacing

To study the effect of grid resolution on the intensity of dust devils, the previously presented simulation HO has been repeated with a grid spacing of 2 m instead of 10 m. This simulation (named HOhr) is almost identical to the simulation comprehensively examined by Raasch and Franke (2011). The main differences are (i) the applied fifth-order advection scheme by Wicker and Skamarock (2002) instead of the second-order scheme by Piacsek and Williams (1970), and (ii) the extended simulation time from 1.5 to 4 hr.

Table 2
Dust Devil Characteristics Derived From Simulation HO

N	$\bar{\tau}$ (s)	$\overline{v_{t_{\mathrm{mean}}}}$ (m/s)	$\overline{r_{\mathrm{mean}}}$ (m)	$\overline{\lvert p\rvert_{\max}}$ (Pa)	$\overline{\lvert\zeta\rvert_{\max}}$ (s^{-1})	$\overline{\langle u_{\tan}\rangle_{\max}}$ (m/s)
861	280 ± 184	0.94 ± 0.40	18.26 ± 3.45	9.01 ± 4.45	0.432 ± 0.094	2.31 ± 0.57
	1,496	2.53	44.55	44.03	0.934	5.54

Note. The second row represents the maximum values with respect to all 861 dust devils fulfilling equation (2). HO = homogeneous.

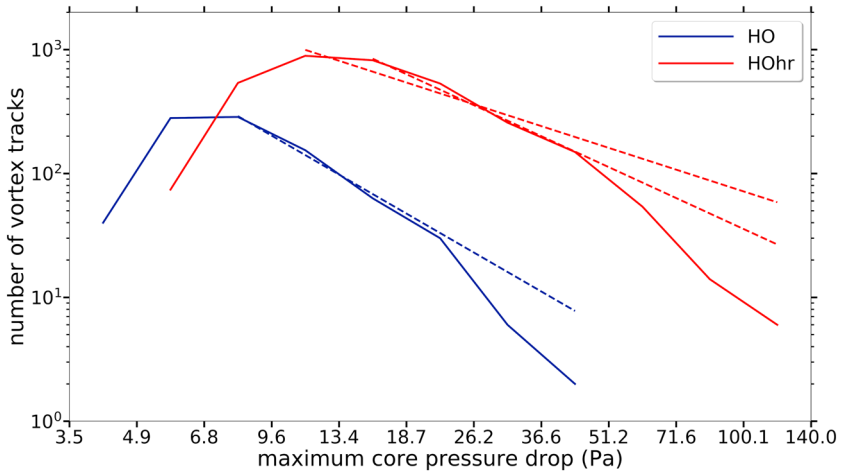

Figure 4. Number of vortex tracks as a function of each track's maximum core pressure drop for simulations HO (blue) and HOhr (red). The dashed lines indicate fitted power laws using nonlinear least squares analysis. For HOhr, two lines are shown, that indicate the different slopes of −1.72 and −1.21 mentioned in the text.

The general dynamics of the CBL, as described for HO, are also apparent in HOhr, including the cellular pattern of convection and the generation of dust devil-like vortices at cell vertices and edges. However, the vortices itself are much better resolved in HOhr, including their dynamics responsible for the generation of a higher core pressure drop. This is shown in Figure 4, which displays the number of vortex tracks (satisfying equation 2) as a function of each track's maximum core pressure drop for both simulations, HO and HOhr. The axes are logarithmically scaled with a bin size ratio of about $\sqrt{2}$ as suggested by Lorenz and Jackson (2016), who argued that this ratio is a good compromise between retaining enough data points to define the function shape while keeping enough counts in each bin to avoid large counting errors. The $\sqrt{2}$ ratio is kept constant in all subsequent plots using logarithmic binning. For HOhr, the most intense dust devils exhibit a factor of 3 higher core pressure drops than in HO, and the total number of dust devil tracks satisfying equation (2) increases by a factor of 4 (from 861 to 3,335). The increased number of vortices is purely related to the better resolution of the dynamics in the CBL and would be even higher if the same detection thresholds (3.5 Pa, 0.087 s^{-1}) had been used. The most intense vortex shows a pressure drop of 138.64 Pa.

The decreasing number of vortex tracks with increasing maximum core pressure drop can be described by a truncated power law starting from the bin with the highest number of detected vortex tracks (e.g., Lorenz & Jackson, 2016; Nishizawa et al., 2016). The power law has the form

$$f(x; a, k) = ax^k, \tag{3}$$

where a and k are constants and x describes the maximum core pressure drop. To fit the function f to the data and determine the coefficients, nonlinear least squares analysis has been used. The resulting curves are also illustrated in Figure 4 revealing a differential power law slope (k value) for the HO data of −2.16 and −1.21 for HOhr (−1.72 if the bin with the second highest number is used as a starting point), which correspond to the range of slopes derived from observational data (−1 to −3; Lorenz, 2014; Lorenz & Jackson, 2016). It has to be noted that the slope heavily depends on the selected starting point and the bin limits which vary from plot to plot to kept the bin ratio constant. If, for example, the maximum number of detected vortex tracks is not pronounced and therefore hard to define, several slopes are conceivable.

Table 3
Dust Devil Characteristics Derived From Simulation HOhr

N	$\bar{\tau}$ (s)	$\overline{v_{t_{mean}}}$ (m/s)	$\overline{r_{mean}}$ (m)	$\overline{\lvert p\rvert_{max}}$ (Pa)	$\overline{\lvert\zeta\rvert_{max}}$ (s^{-1})	$\overline{\langle u_{tan}\rangle_{max}}$ (m/s)
3,335	210 ± 105	1.08 ± 0.39	4.69 ± 1.52	17.70 ± 11.91	2.76 ± 0.78	3.03 ± 0.57
	995	2.75	26.06	138.64	7.76	9.0

Note. The second row represents the maximum values with respect to all 3,335 dust devils fulfilling equation (2).

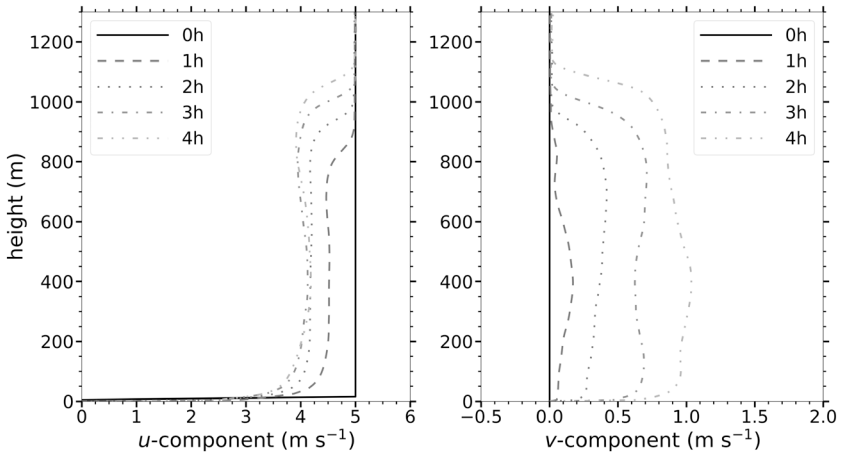

Figure 5. Horizontally and temporally averaged profiles of the horizontal velocity components u (left) and v (right) for five different simulation times derived from HOu5.

Table 3 lists the most important statistical quantities for simulation HOhr, showing much higher values of the averaged pressure drop maximum, vorticity maximum, and tangential velocity maximum compared to HO. This consistent behavior can be well described by theoretical models like the Rankine vortex or Burgers-Rott vortex model that put pressure drop, vorticity, and tangential velocity in relation (e.g., Alekseenko et al., 2007). The mean radius averaged over all detected vortices is much smaller compared to HO but can be still described with about two grid points. The changes in the mean translation speed are comparatively low, whereas the averaged lifetime of a dust devil decreases from 280 to 210, which can be attributed to the different detection thresholds in HO and HOhr as well as to the better resolution of small-scale, short-lived structures. Finally, the confidence interval of the averaged pressure drop maximum is [17.29 Pa, 18.10 Pa].

The comparison between HO and HOhr shows that it is mandatory to decrease the grid spacing for a successful simulation of dust devils. An even further reduction of the grid spacing might result in even higher core pressure drops. This claim is supported by analyzing power spectral densities of the perturbation pressure, potential temperature, and velocity components (not shown). The combination of the subgrid-scale model dissipation and the numerical dissipation of the advection scheme strongly damps spatial scales less than 4 times the grid spacing. Therefore, fluctuations on a scale of several meters are still heavily damped in simulations with 2-m grid spacing, which requires even finer resolutions for an accurate study of dust devils. For example, ultrahigh resolution dust devil simulations with a grid spacing of 0.1 m performed by Gu et al. (2008) reproduced core pressure drops of 200 Pa. However, these simulations are not able to cover the generation of dust devils by the dynamics of the boundary layer due to limited computing capabilities restricting the modeling domain to a couple of hundreds of meters horizontally. Also in our study, computing capabilities prohibit a further reduction of grid spacing (e.g., the HOhr simulation demands 23-hr CPU time on 6400 cores of a CRAY-XC40), and even a grid spacing of 2 m is too expensive for all simulations of this study. Accordingly, we will receive our main conclusions on the effects of background wind and heterogeneities on the strength of dust devils from simulations using a 10-m grid spacing, before we return to a 2-m grid spacing for the final simulation of our study.

3.3. The Effect of Background Wind

Previous studies suggest that light background winds are beneficial to dust devil formation in numerical models (e.g., Raasch & Franke, 2011) and in the real atmosphere (e.g., Rafkin et al., 2016). A further increase in background wind, however, turns the convective cells to a band-like pattern, therefore, inhibiting the formation of dust devils (Raasch & Franke, 2011; Sinclair, 1969). To quantify the effect of background wind on dust devil intensity, we impose different geostrophic winds of 2.5, 5.0, 7.5, and 10.0 m/s in x direction (simulations HOu2.5, HOu5, HOu7.5, and HOu10).

In Figure 5, the evolving horizontally and temporally averaged vertical profiles of the horizontal wind components are shown exemplarily for a geostrophic wind of 5.0 m/s.

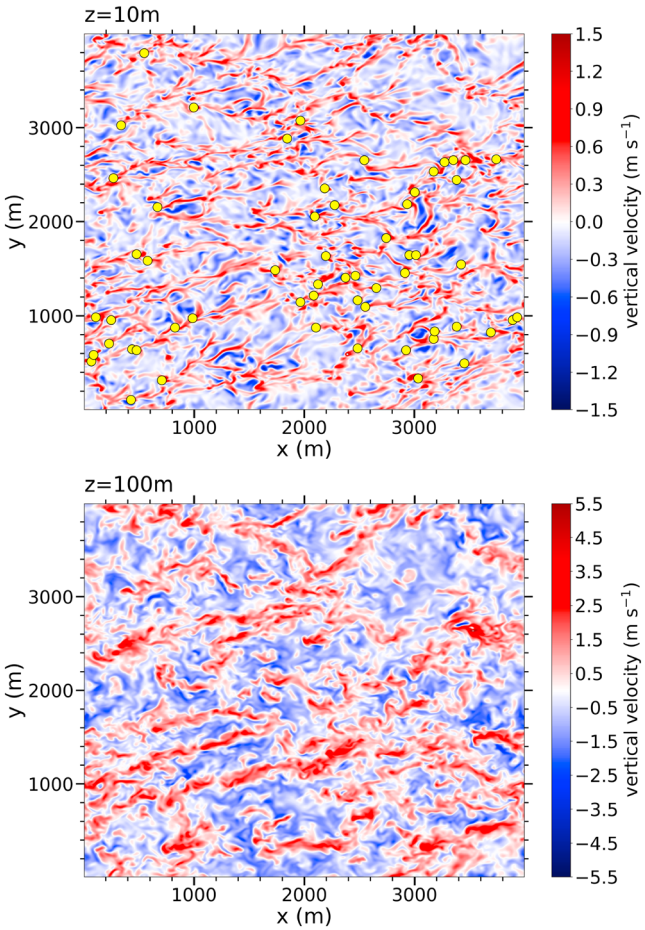

Figure 6. Horizontal cross sections of the instantaneous vertical velocity at 10 m (top) and 100 m (bottom) height after 10,800-s simulated time derived from simulation HOu7.5. Detected vortex centers are depicted as yellow dots.

The profiles indicate again a well-mixed boundary layer growing in time. Wind shear, known to significantly influence dust devil development (e.g., Balme et al., 2003), is mainly apparent close to the ground and in the entrainment zone near the inversion height. Above, the geostrophic balance is fulfilled. Furthermore, the wind direction changes according to the Ekman spiral from *x* axis parallel (270°) above the inversion height to roughly 255° close to the ground (after 4 hr). The profiles of HOu2.5, HOu7.5, and HOu10.0 show a similar behavior.

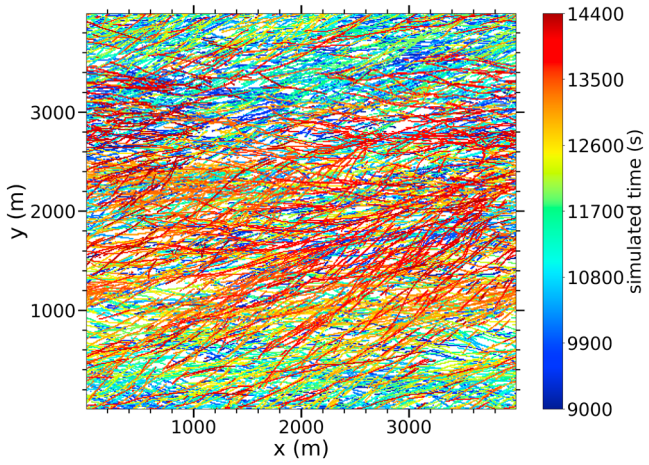

Figure 7. Spatial distribution of all 9,111 vortex tracks between 9,000 and 14,400 s derived from simulation HOu5. Each vortex center is represented by a dot. The color of the dot codes the simulated time at detection.

For a geostrophic wind of 5.0 m/s, the vertical velocity exhibits a similar convective cell pattern as shown in Figure 2 with vortex centers at the vertices and branches of the cells. For a weaker geostrophic wind of 2.5 m/s (simulation HOu2.5) the convective cell pattern is more pronounced than in simulation HOu5 (not shown), while for stronger geostrophic winds of 7.5 and 10.0 m/s the cell pattern is completely blurred and structures appear to be elongated along the *x* direction (Figure 6 for HOu7.5).

The vortices move approximately in the direction of the mean near-surface wind during the course of their lifetime. Thus, convective cells (well pronounced in Figure 3) are blurred here completely, which can be also seen from the spatial distribution of dust devil tracks derived from simulation HOu5 (Figure 7). The averaged translation direction is 253°. However, a single vortex can have deviations from the mean surface wind direction of more than 30°, with a standard deviation of migration

Table 4
Dust Devil Characteristics Derived From Simulation HOu2.5, HOu5, HOu7.5, and HOu10

Simulation name	N	$\bar{\tau}$ (s)	$\overline{v_{t_{mean}}}$ (m/s)	$\overline{r_{mean}}$ (m)	$\overline{\lvert p\rvert_{max}}$ (Pa)	$\overline{\lvert\zeta\rvert_{max}}$ (s^{-1})	$\overline{\langle u_{tan}\rangle_{max}}$ (m/s)
HOu2.5	1,460	280 ± 190	2.1 ± 0.67	22.01 ± 5.50	10.18 ± 5.46	0.438 ± 0.106	2.40 ± 0.63
		1,656	4.37	55.10	52.15	0.944	5.71
HOu5	1,889	258 ± 150	3.94 ± 0.75	26.37 ± 6.79	11.61 ± 6.03	0.438 ± 0.107	2.54 ± 0.65
		1,398	6.11	81.20	51.06	0.947	5.78
HOu7.5	1,143	214 ± 98	5.73 ± 0.77	29.30 ± 7.38	12.55 ± 6.78	0.440 ± 0.111	2.63 ± 0.68
		889	9.33	70.0	54.57	0.933	5.61
HOu10	536	181 ± 61	7.21 ± 0.8	30.87 ± 9.28	14.25 ± 7.59	0.464 ± 0.118	2.85 ± 0.70
		593	9.81	71.85	51.42	0.910	5.59

Note. The second row of each conducted simulation represents the maximum values with respect to all N tracked dust devils fulfilling equation (2).

direction of 13.92° (HOu2.5), 8.20° (HOu5), 6.55° (HO7.5), and 6.61° (HOu10). This agrees with observations of Lorenz (2016), who showed that dust devil migration directions follow the ambient wind but with a standard deviation described by $\arctan(R/U)$ with U being the ambient wind speed and R being a constant that depends on the regarded data set.

The total number of detected vortex tracks between 9,000 and 14,400 s is much higher for simulation HOu5 (9,111) than those for HO (1,952) and HOu2.5 (4,309) but still less than the number for HOu7.5 (14,226) or HOu10 (23,882) indicating that even stronger background winds trigger the development of vertical vortices. This is because of the increased near-surface wind shear, whereby additional horizontal vorticity is generated, which is then tilted into vertical vorticity via the twisting term (see Raasch & Franke, 2011). At the same time, vortices become more and more unstable due to higher turbulence that occur together with higher background winds. Further turbulence then favors the decay of coherent structures like dust devils, which results in shorter averaged lifetimes (see the bulk characteristics in Table 4). As explained by Raasch and Franke (2011), the decrease of longer-lasting, well-developed dust devils can be additionally explained by the more shear-dominated conditions, which inhibit persistent, convective cells essentially needed for the generation and maintenance of dust devils.

The interaction between reduced averaged lifetimes and increased total numbers of vortex tracks in case of higher background winds is illustrated in Figure 8, which shows the cumulative number of vortex tracks having a lifetime greater or equal to the respective value on the x axis. It can be seen that no- and low-wind

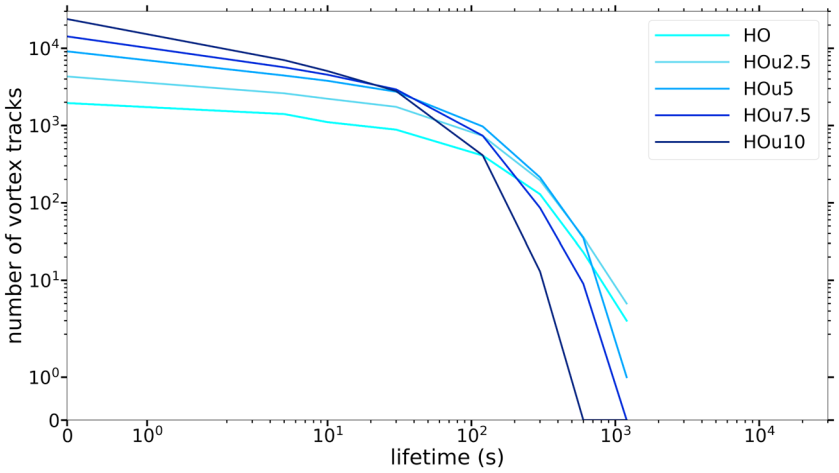

Figure 8. Cumulative number of vortex tracks between 9,000 and 14,400 s as a function of the vortices' lifetime for simulations HO, HOu2.5, HOu5, HOu7.5, and HOu10. The colors were chosen in a way that higher wind speeds have darker blue tones.

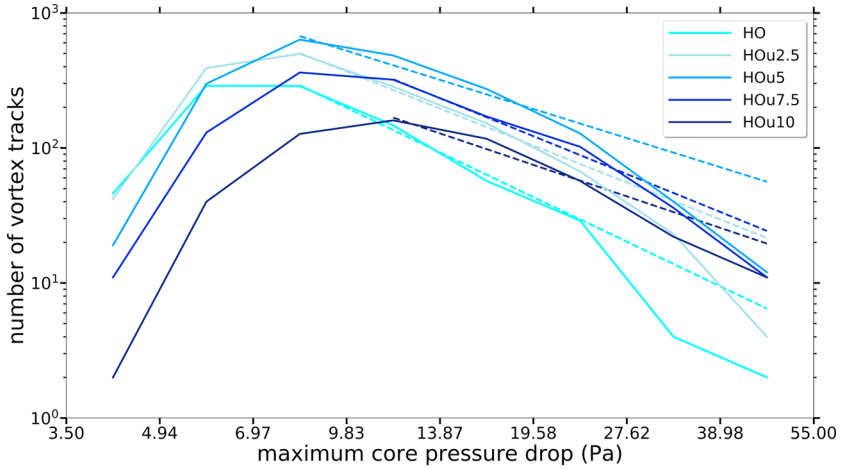

Figure 9. Number of vortex tracks as a function of each track's maximum core pressure drop for simulations HO, HOu2.5, HOu5, HOu7.5, and HOu10. The colors were chosen in a way that higher wind speeds have darker blue tones. The dashed lines indicate fitted power laws using nonlinear least squares analysis.

situations produce more longer-lasting vortices than under strong-wind conditions. For short-lived vortices, the exact opposite is the case.

Table 4 also shows that the impact of the background wind velocity on the number of detected vortex tracks satisfying equation (2) is less distinct. For a moderate increase of the background wind of 2.5 and 5.0 m/s the number of tracks (1,460 for HOu2.5 and 1,889 for HOu5) increases by a factor of about 2 in comparison to the windless simulation HO (861). For stronger background winds of 7.5 or 10.0 m/s the number of tracks decreases drastically to 1,143 and 536, respectively. This behavior is a consequence of both effects described above: an increasing total number of detected tracks accompanied by decreasing averaged lifetimes at higher background winds. For winds up to 5 m/s the increase of tracks is more pronounced in the statistically analyzed data than the decline in lifetime. Therefore, the number of tracks with a duration of at least 120 s increases, too. For geostrophic winds above 5 m/s, however, the overall increase of tracks is less pronounced than the decline in lifetime, which results in lower values for N.

The quantitative impact of different background winds on the maximum core pressure drop occurring during each track is presented in Figure 9 (for excat values see Table 4). The plots' average maximum core pressure drop increases from 9.01 to 10.18, 11.61, 12.55, and 14.25 Pa having confidence intervals of [8.71 Pa, 9.30 Pa], [9.90 Pa, 10.46 Pa], [11.34 Pa, 11.88 Pa], [12.16 Pa, 12.94 Pa], and [13.61 Pa, 14.89 Pa] for the simulations HO, HOu2.5, HOu5, HOu7.5, and HOu10, respectively. This shows that higher background winds result in more intense vortices, shifting the maximum number of detected vortex tracks to higher maximum core pressure drop values. The higher relative number of intense vortices can be explained by the increased near-surface shear due to stronger background winds, whereby the horizontal component of rota-

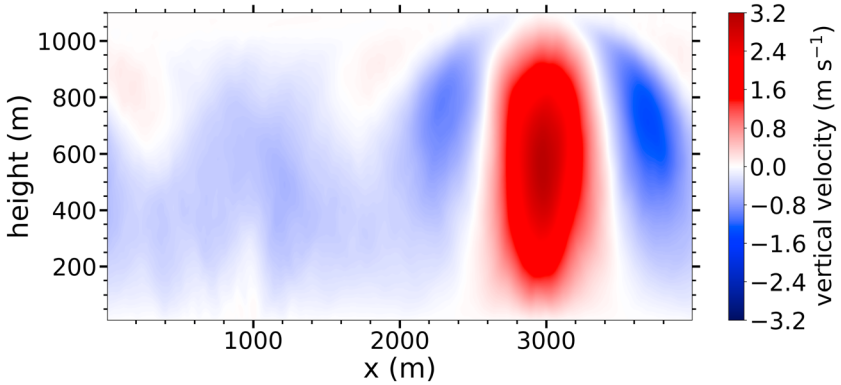

Figure 10. Vertical cross section of vertical velocity at 10,800 s, averaged along y and over the previous 900 s for simulation HE.

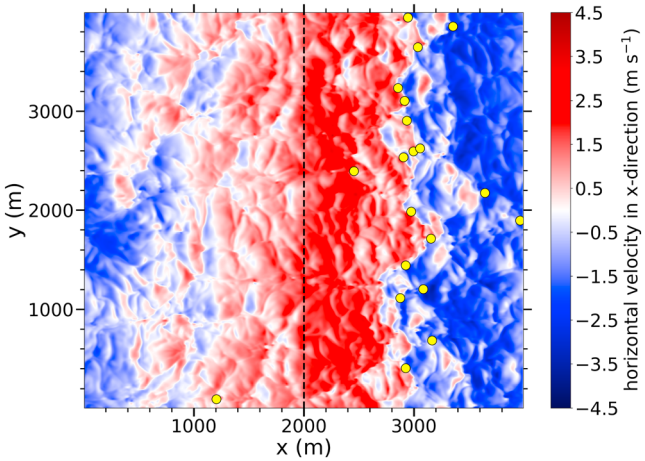

Figure 11. Horizontal cross section of the u component of the horizontal velocity at 5-m height and at 10,800-s simulated time for simulation heterogeneous. The dashed line represents the border between the differently heated areas (left: less heated, right: stronger heated). Detected vortex centers are depicted as yellow dots.

tion increases, which contributes via the twisting term to larger vorticity, dust devil tangential velocity, and pressure drop values (see Table 4 and Raasch & Franke, 2011). In addition, the total maximum core pressure drop increases compared to HO but does not change significantly with background wind. The combination of a nearly constant total maximum pressure drop with an increased number of intense vortices within the population results in less steep differential power law slopes of −2.21 (HO), −1.83 (HOu2.5), −1.44 (HOu5), −1.26 (HOu7.5, −1.88 if the bin with the second highest number is used as indicated in Figure 9), and −1.56 (HOu10). A meaningful comparison to observational data is still pending due to missing database.

All in all, high background winds are beneficial to the production of more intense vortices, but the number of long-living vortex tracks (several minutes) decreases drastically if a certain threshold velocity is exceeded. Therefore, light or moderate background winds, as they are typically present in regions of high dust devil occurrence (Jemmett-Smith et al., 2015), should be also included in future LES of dust devils to represent their observed intensity more accurately.

3.4. The Effect of Heterogeneities

To quantify the effect of heterogeneities on the intensity of dust devils, a striped pattern of heating is imposed in simulation HE: The left half of the model domain's surface (0 m ≤ x < 2,000 m) is heated with a surface

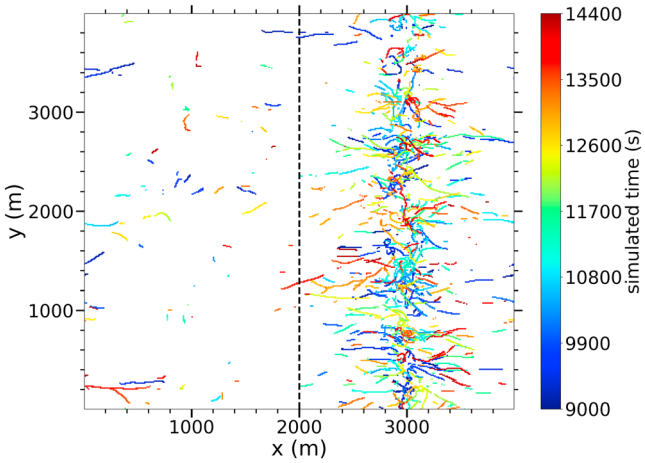

Figure 12. Spatial distribution of all 1,298 vortex tracks between 9,000 and 14,400 s derived from simulation HE. Each vortex center is represented by a dot. The color of the dot codes the simulated time at detection. The dashed line represents the border between the differently heated areas.

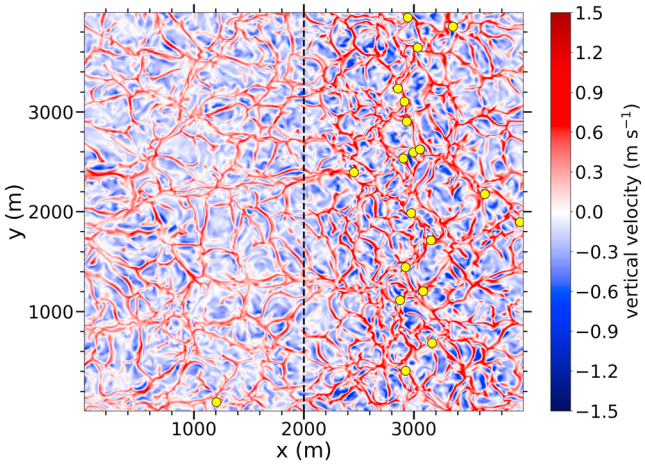

Figure 13. Horizontal cross sections of the instantaneous vertical velocity at 10-m height after 10,800-s simulated time derived from simulation HE. Detected vortex centers are depicted as yellow dots. The dashed line represents the border between the differently heated areas.

heat flux of 0.12 K·m·s^{-1} and the right part (2,000 m $\leq x <$ 4,000 m) with 0.36 K·m·s^{-1}, resulting in the same net surface heat flux of 0.24 K·m·s^{-1} as applied in all previously presented simulations of this study.

Due to this differential heating, a secondary circulation develops (e.g., Avissar & Schmidt, 1998; Letzel & Raasch, 2003), in which air rises above the stronger heated region ($x = 3,000$ m) and sinks above the less heated region ($x = 1,000$ m, Figure 10). Due to mass continuity, this pattern is associated with a low-level convergence line above the stronger heated region, where dust devil centers seem to cumulate (Figure 11). Keep in mind that due to the staggered grid used in PALM, the horizontal velocity components are vertically shifted by half the grid spacing. Therefore, Figure 11 shows the horizontal cross section of the u component in 5 m and not in 10 m.

The spatial distribution of vortex tracks (Figure 12) indicates that dust devils are mostly generated over the stronger heated area close to the convergence line and are then advected toward it. Because the heating might not be sufficient for the development of dust devils, only a negligible amount is generated in the less heated region. Indeed, the upward vertical velocities associated with the cell edges and vertices (Figure 13) are lower in the less heated region than in the stronger heated region, making the less heated region less favorable for the development of dust devils. Moreover, the cells above the stronger heated region are more dense than above the less heated region, containing more vertices responsible for generating dust devils. This compression is a result of the secondary circulation, which low-level convergence compacts the cells above the stronger heated region, whereas the low-level divergence broadens the cells above the less heated area.

The number of detected vortex tracks with a lifetime >120 s decreases by about 50% for HE in comparison to HO, which is mainly due to geometric reasons (area of intense heating is halved, Table 5), and the secondary circulation: The subsidence of air together with the small magnitude of the heat flux over the less heated region prevents the development of dust devils, whereas dust devils are triggered along the convergence line and by the high heat flux above the stronger heated region more frequently. The stimulation of vertical vortices along the convergence line is mainly due to the fact that air parcels flowing toward each other tend to produce rotation in a horizontal plane and, consequently, vortices with a vertical axes.

Table 5
Dust Devil Characteristics Derived From Simulation HE

N	$\bar{\tau}$ (s)	$\overline{v_{t_{mean}}}$ (m/s)	$\overline{r_{mean}}$ (m)	$\overline{\lvert p\rvert_{max}}$ (Pa)	$\overline{\lvert\zeta\rvert_{max}}$ (s^{-1})	$\overline{\langle u_{tan}\rangle_{max}}$ (m/s)
463	300 ± 256	1.09 ± 0.53	21.19 ± 4.72	11.15 ± 7.23	0.485 ± 0.125	2.61 ± 0.75
	2,163	2.95	47.24	60.26	1.097	6.03

Note. The second row represents the maximum values with respect to all 463 dust devils fulfilling equation (2). HE = heterogeneous.

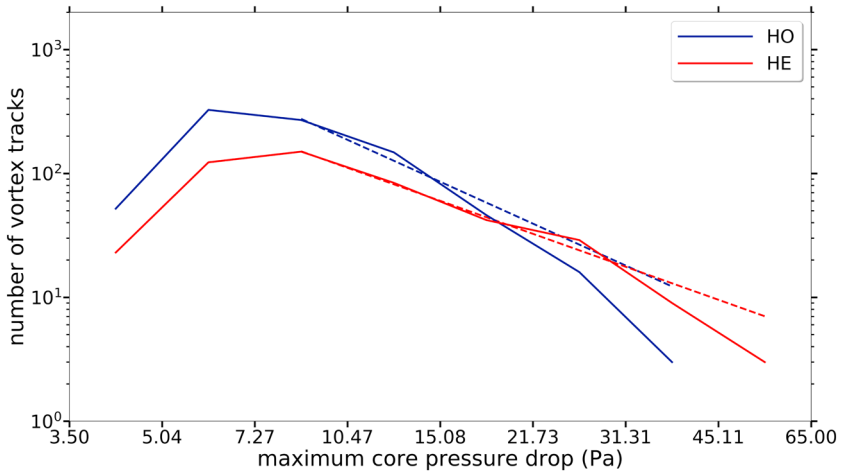

Figure 14. Number of vortex tracks as a function of each track's maximum core pressure drop for simulations HO (blue) and HE (red). The dashed lines indicate fitted power laws using nonlinear least squares analysis. HE = heterogeneous; HO = homogeneous.

The mean lifetime, translation speed, and radius values do not change significantly compared to HO (a little higher values for HE). However, the mean of the maximum core pressure drop increases from 9.01 Pa for HO to 11.15 Pa for HE with a confidence interval of [10.49 Pa, 11.81 Pa], indicating that more intense vortices are produced in simulation HE. This is additionally supported by a higher overall maximum of the pressure drop, increasing from 44.03 Pa (HO) to 60.26 Pa (HE). The more intense vortices during simulation HE are caused by the higher sensible surface heat flux in the stronger heated region, which directly produces stronger vortices as theoretical models of Renno and Ingersoll (1996) and Renno et al. (2000), and Renno et al. (1998) suggest. Additionally, the secondary circulation induces a low-level wind that is favorable for the production of more intense vortices due to additional shear similar to the simulations with an imposed geostrophic wind (see section 3.3). Consequently, the dust devil's vorticity and tangential velocity values increase.

The line plot shown in Figure 14 underlines again the production of more intense vortices in HE compared to HO. Although only half as many dust devils as in HO were recorded, the number of dust devils for the bins with high maximum core pressure drops increases significantly compared to HO. In total, the core pressure drop data can be approximated with slopes of −1.38 (HO, −2.13 if the bin with the second highest number is used as indicated in Figure 14) and −1.68 (HE).

To isolate the effect of the secondary circulation from the higher surface heat flux in one half of the modeling domain, a homogeneous simulation with a sensible surface heat flux of 0.36 $K \cdot m \cdot s^{-1}$ was conducted (HOhf, results not shown). If the increased surface sensible heat flux was the only reason for the increased vortex strength, more stronger vortices than in simulation HE would occur because the surface heating of 0.36 $K \cdot m \cdot s^{-1}$ covers the whole model domain instead of the half as in simulation HE. However, though more and stronger vortices occur in HOhf than in the homogeneous simulation with a net sensible surface heat flux of 0.24 $K \cdot m \cdot s^{-1}$ (HO), there is no significant difference concerning the mean maximum core pressure drop between the stronger heated homogeneous (HOhf, 11.35 Pa ± 6.52 Pa, confidence interval of [11 Pa, 11.35 Pa]) and the heterogeneous simulation (HE, 11.15 Pa ± 7.23 Pa, confidence interval of [10.49 Pa, 11.81 Pa]). In fact, the overall maximum pressure drop in HE (60.26 Pa) is even higher than in simulation HOhf (55.57 Pa). Thus, it can be concluded that the structure of the surface heating and the resulting secondary circulation has a significant impact on the formation of vortices by allowing the development of stronger dust devils.

Another variable probably affecting the generation of vortices is the width of the surface heterogeneity. To address this, additional simulations with a striped pattern and a width of 2 km (HE2), 8 km (HE8), and 16 km (HE16) have been conducted (results not shown). Simulation HE2 has the same horizontal domain like HO (4 km × 4 km), while the simulations HE8 and HE16 have a horizontal domain of 8 km × 4 km and 16 km × 4 km, respectively, to capture the larger strip widths. In simulation HE2 the vortices are weaker in comparison to the above-described simulation with a width of 4 km (HE), whereas stronger vortices appear for

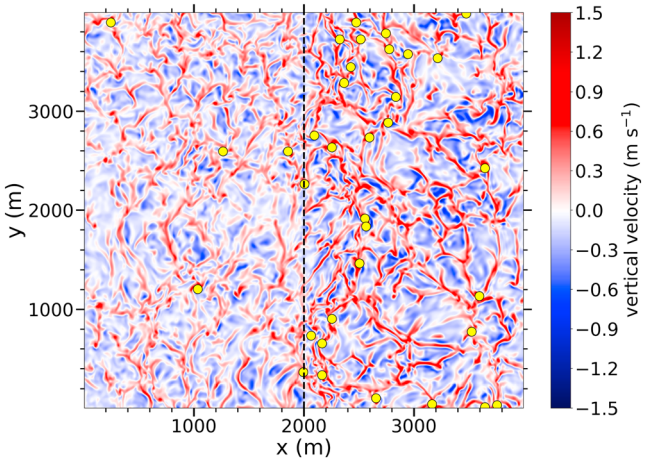

Figure 15. Horizontal cross sections of the instantaneous vertical velocity at 10-m height after 10,800-s simulated time derived from simulation HEv5. Detected vortex centers are depicted as yellow dots. The dashed line represents the border between the differently heated areas.

stripes of 8 km (HE8) and even stronger ones for stripes of 16 km (HE16), which is in agreement with previous studies showing that the secondary circulation intensifies with increasing width (Avissar & Schmidt, 1998; Letzel & Raasch, 2003; Shen & Leclerc, 1995).

3.5. The Effect of Background Wind on a Heterogeneous Simulation

By imposing an additional background wind on a heterogeneously heated simulation, it is expected to combine the effects of heterogeneity and wind, resulting in even stronger vortices. For this reason, we extended the setup of the heterogeneously heated simulation HE with a geostrophic wind of 5 m/s to test this hypothesis (simulation HEv5). In contrast to the homogeneous simulations, the direction of the background wind matters. A background wind perpendicular to the heterogeneity would weaken the secondary circulation (e.g., Avissar & Schmidt, 1998; Letzel & Raasch, 2003) and the effect on dust devils. Therefore, the background wind is imposed parallel to the heterogeneity (i.e., in positive y direction).

In simulation HEv5 a secondary circulation and a convective cell pattern similar to simulation HE develop, but with structures more and more aligned along the y axis (see Figure 15). In addition, less intense convective cells occur over the less heated patch. Due to the additionally considered background wind, the low-level convergence line shifts to the left during the simulation (not shown). This is a result of the Coriolis force, generating a negative u component at the surface that accelerates with time (see Figure 5). As

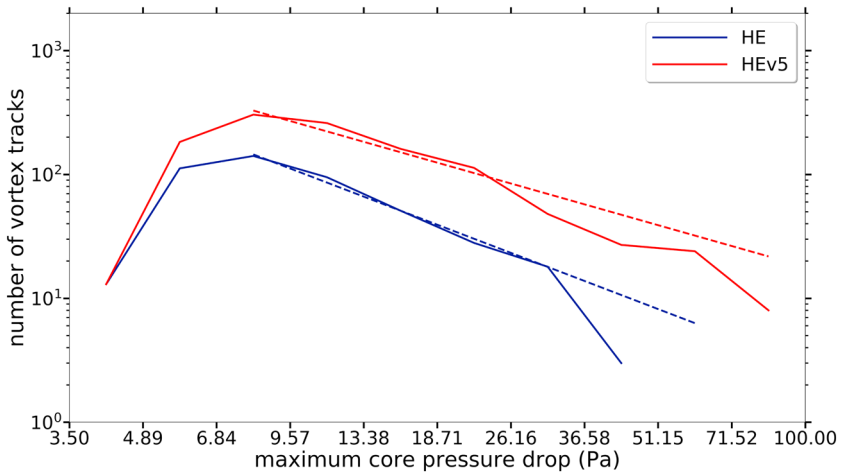

Figure 16. Number of vortex tracks as a function of each track's maximum core pressure drop for simulations HE (blue) and HEv5 (red). The dashed lines indicate fitted power laws using nonlinear least squares analysis. HE = heterogeneous.

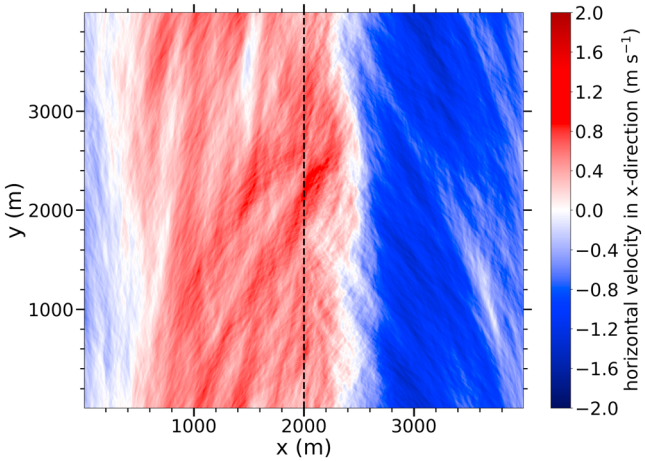

Figure 17. Horizontal cross section of the u component of the horizontal velocity (averaged over the previous 900 s) at 5-m height and at 10,800-s simulated time for simulation HEv5hr. The dashed line represents the border between the differently heated areas.

in the previous simulations, most vortices are located at the cell edges and vertices. Besides, the vortices are primarily generated above the stronger heated region and are advected toward the convergence line of the secondary circulation (as in simulation HE). In addition to the movement in x direction caused by the secondary circulation, the vortices also move with the imposed background wind in y direction.

Figure 16 shows the number of detected vortex tracks having a certain maximum core pressure drop for simulations HE and HEv5. The total number of vortices with a duration of at least 120 s is larger in simulation HEv5 (1141) than in simulation HE (463) due to the overall increase of tracks by the additional shear as a result of the background wind (see discussion in section 3.3). The occurrence of intense vortices also increases in simulation HEv5, which is indicated by the mean maximum core pressure drop, which increases from 11.15 Pa for simulation HE to 14.25 Pa for simulation HEv5, with a confidence interval of [13.58 Pa, 14.93 Pa] and with the strongest vortex in HEv5 having a core pressure drop of 95.44 Pa. Additionally, Figure 16 displays differential power law slopes of −1.56 for HE and −1.16 for HEv5. The changes in the other dust devil characteristics caused by a moderate background wind in a heterogeneous environment demonstrate a similar picture as those already discussed in section 3.3, where a geostrophic wind of 5 m/s was imposed on simulation HO.

3.6. Combined Effect of All Factors Enhancing Vortex Strength

As shown in the previous subsections, the physical parameters of background wind and surface heterogeneity and a high spatial resolution as a numerical parameter enhance the strength of simulated vortices. Now, we combine all parameters in a final simulation, that is, a heterogeneous surface with a striped pattern of 4-km width, a background wind of 5 m/s parallel to the pattern of heating, and a high spatial resolution of 2 m.

Figure 17 shows the location of the convergence line for simulation HEv5hr in a horizontal cross section of the u component at a height of 5 m after 10,800-s simulated time. As in simulation HEv5, the convergence line of the secondary circulation is shifted to the left during the simulation. At the end of the simulation, the convergence line is located close to the border of the differently heated areas.

The convective cell pattern at the first grid point above the surface is less pronounced in HEv5hr compared to HEv5 (see Figure 18). In HEv5hr, much more finer structures are resolved, which appear as streaks mostly orientated along y due to the imposed background wind. However, the displayed height is 2 m instead of 10 m, which makes a direct comparison to Figure 15 difficult. For example, small structures, which occur in particular just above the surface, are only represented in horizontal cross sections extracted at several meters height. Nevertheless, the usage of 2 m as the analysis height is much more meaningful since observations of parameters describing dust devils are mainly carried out at height levels less than 10 m (e.g., Metzger et al., 2011; Tratt et al., 2003). Further away from the surface (100 m), the cellular structure is also strongly modified by the background wind and the secondary circulation. Besides, vortices are again mainly located over the stronger heated area close to the current position of the convergence line, where strong updrafts

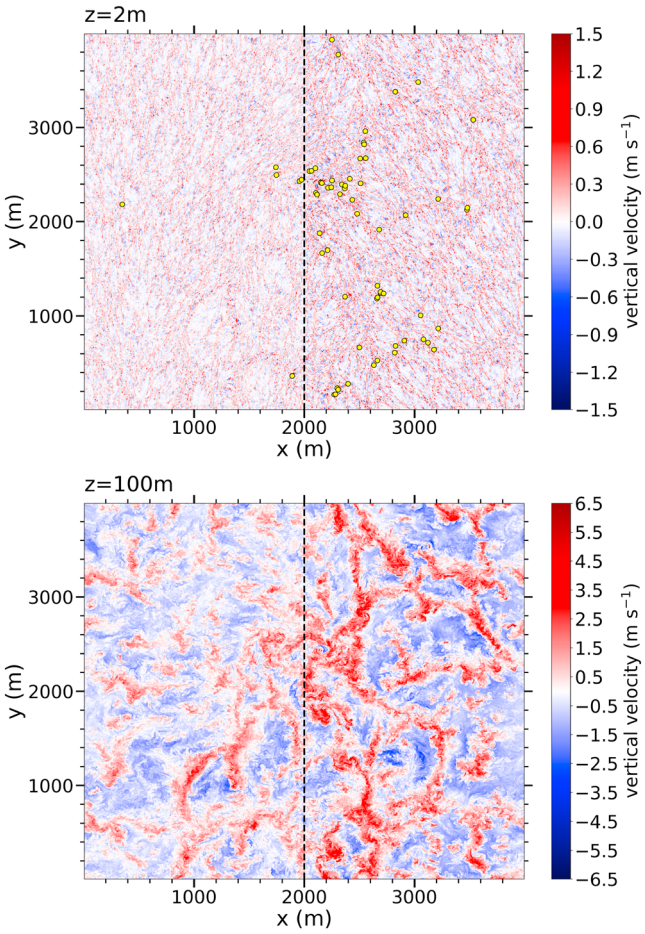

Figure 18. Horizontal cross sections of the instantaneous vertical velocity at 2-m (top) and 100-m (bottom) height after 10,800-s simulated time derived from simulation HEv5hr. Detected vortex centers are depicted as yellow dots.

occur and structures are merging. After the generation of the vortices, they are advected toward the low-level convergence line (not shown).

The distribution of the maximum core pressure drop is given in Figure 19 showing a quite gradual differential power law slope of −0.96 due to the lack of very strong and long-living vortices. Nevertheless, vortices are much stronger than in all previous simulations. Two vortices occur with a maximum core pressure drop of more than 200 Pa, with the strongest vortex having a value of 218.93 Pa, which is very close to the range of observed intensities (250 to 450 Pa, Kanak, 2005, 2006; Sinclair, 1973). Besides the increased vortex strength, the number of detected vortex tracks with a duration of at least 120 s decreases substantially (193), which supports the findings of Raasch and Franke (2011), where for the 2-m run in combination with a background wind of 5 m/s significantly less centers and well-developed tracks than in all other runs were detected. The strong decrease of dust devil-like structures was not really expected because of the 2.5 times higher number in simulation HEv5 compared to HE and more dust devil detections during the high-resolution run presented in section 3.2. Anyhow, the reason for the low number of detected vortex tracks with a duration of at least 120 s is, first, the reduced averaged lifetime of dust devil-like vortices for high-resolution runs as discussed in section 3.2. This counteracts the overall increase of vortices with decreasing grid spacing. Second, values of 120 s and more belong to the longest registered lifetimes (not shown). At such lifetimes, a further increase in background wind reduces the number of tracks (see Figure 8). Moreover, the secondary circulation can also be interpreted as an additional background wind, which reduces the number of vortices with a lifetime of at least 120 s even further.

Finally, Table 6 gives an overview of dust devil characteristics. For HEv5hr, the interaction of the high resolution, background wind, and secondary circulation result in shorter lifetimes than for HEv5 (as explained

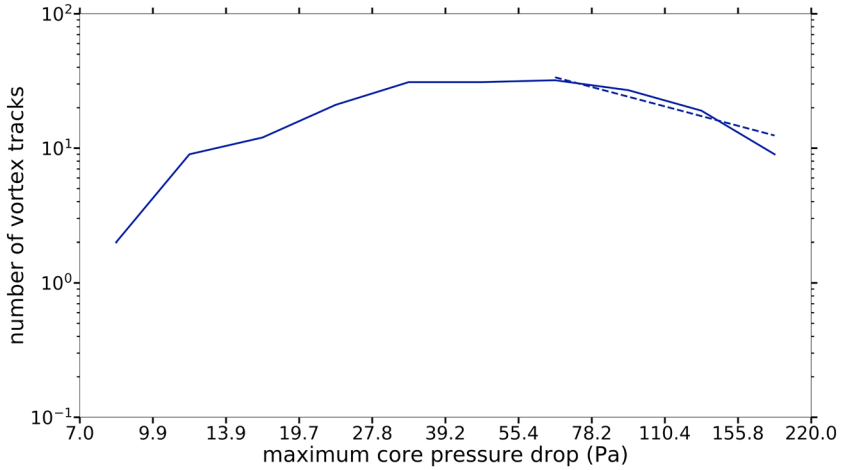

Figure 19. Number of vortex tracks as a function of each track's maximum core pressure drop for simulation HEv5hr. The dashed line indicates a fitted power law with a slope of −0.96 using nonlinear least squares analysis.

above). However, lifetimes around 200 s (several minutes) still agree well with observations (Balme & Greeley, 1998). The migration velocity resembles the ones of simulation HEv5 and HOu5, whereas the mean radius is much smaller due to the finer resolution. In line with the pressure, also mean vorticity and tangential velocity values increases a lot compared to HEv5. The confidence level of the mean maximum core pressure drop is [56.76 Pa, 69.27 Pa].

Run HEv5hr was repeated but with slightly different initial conditions with respect to the random perturbations, which were imposed on the horizontal velocity field in the beginning (see section 2.1). That way, the statistics of dust devils for HEv5hr could be improved. All in all, three vortices occur with a maximum core pressure drop of more than 250 Pa, with the strongest vortex having a value of 306.17 Pa, which is well in the range of observed intensities (250 to 450 Pa, Kanak, 2005, 2006; Sinclair, 1973). Note that these three vortices are the first simulated vortices as intense as observed dust devils.

4. Summary and Conclusion

The purpose of this study was to examine the effect of grid spacing, background wind, and surface heat flux heterogeneities on simulated dust devil-like vortices with the aim of simulating vortices as strong as observed in nature. Though previous studies could successfully reproduce the characteristic structure of dust devils, the core pressure drop of the simulated vortices was almost 1 order of magnitude too small (e.g., Cortese & Balachandar, 1993; Gheynani & Taylor, 2010; Ito et al., 2013; Kanak et al., 2000; Raasch & Franke, 2011).

As a first step, we analyzed the effect of the LES model resolution. Due to an increased resolution of the vortex microstructure, dust devil-like vortices are more numerous and the core pressure drop is more intense, which is in accordance with a previous study by Raasch and Franke (2011).

Another factor known to enhance vortex strength is an imposed background wind (e.g., Raasch & Franke, 2011; Sinclair, 1969). While Raasch and Franke (2011) found a background wind of 2.5 m/s to cause the largest increase in vortex strength, this study shows that the ideal wind speed concerning the averaged vortex strength seems to be higher (though the exact optimum wind speed was not determined). However, the

Table 6
Dust Devil Characteristics Derived From Simulation HEv5hr

N	$\bar{\tau}$ (s)	$\overline{v_{t_{mean}}}$ (m/s)	$\overline{r_{mean}}$ (m)	$\overline{\lvert p\rvert_{max}}$ (Pa)	$\overline{\lvert\zeta\rvert_{max}}$ (s^{-1})	$\overline{\langle u_{tan}\rangle_{max}}$ (m/s)
193	200 ± 93	3.86 ± 0.72	5.37 ± 1.66	63.02 ± 44.06	5.01 ± 1.81	5.66 ± 2.02
	729	5.63	17.40	218.93	9.78	11.28

Note. The second row represents the maximum values with respect to all 193 dust devils fulfilling equation (2).

number of detected dust devils lasting several minutes decreases drastically if a certain wind speed threshold is exceeded.

Heterogeneous surfaces, which are found in observations to increase vortex strength (Renno et al., 2004; Sinclair, 1969), were never before considered in numerical simulations of dust devils. We examined the effect of a 1-D striped heating pattern. Due to a developing secondary circulation (e.g., Avissar & Schmidt, 1998), the convective cells over the stronger heated area are more intense and compact, leading to an increase in vortex strength. Interestingly, the simulation shows that dust devils accumulate at the low-level convergence line above the stronger heated region and not at the border of surface heterogeneities as observations suggest (Renno et al., 2004; Sinclair, 1969). Since this study has only focused on heat flux heterogeneities and not on roughness heterogeneities, which might be the more significant heterogeneity in the above-mentioned observations, further investigations are necessary.

A final simulation combined all previously studied effects. The simulation featured a grid resolution of 2 m, a background wind of 5 m/s, and a surface heating heterogeneity. The combination of all features leads to a significant increase in dust devil intensity. It also leads to a maximum core pressure drop of 306 Pa, which agrees well with observed values ranging from 250 to 450 Pa. This simulation is the first to produce dust devil-like vortices with observed intensities.

However, this study should be seen as a first step toward the simulation of dust devils with observed intensity. Individual influences, especially that of heterogeneities introducing baroclinity and hence an additional source of vorticity, need to be investigated more carefully in follow-up studies. Due to the erratic occurrence of dust devils, future studies should also extend the model domain or simulation time, which have been limited in this study due to computational restrictions. In this way, the statistics on dust devils intensity can be improved, especially with respect to the strongest and therefore rarest dust devils. Also, an ensemble-based approach would improve the statistics even further. However, the general tendencies of grid spacing, background wind, and surface heat flux heterogeneities on the intensity could be shown clearly.

In the future, we want to investigate the statistics of dust devils with observed intensity in more detail. Especially, the three-dimensional structure, correlations between dust devil features, the initial generation process, and the mechanism of maintaining dust devils will be addressed by using a nesting technique, which has been recently implemented in PALM and which will allow for near-surface grid spacings of 1 m and below. Our future studies will also incorporate laboratory studies to represent atmospheric convection and hence dust devil-like structures. The barrel of Ilmenau, which is a large-scale experimental facility to investigate turbulent convection, will be an appropriate environment for these studies (e.g., du Puits et al., 2013). Such a controlled environment will allow the derivation of similar statistics as done in the simulations presented here (and which are almost impossible to derive in a real-world environment). By comparing dust devil-like structures in simulations and laboratory, we will be able to identify and to understand distinct differences and, if necessary, figure out appropriate ways to improve our simulations toward reality even further.

Acronyms

CBL Convective boundary layer
LES Large-eddy simulation
PALM The Parallelized Large-Eddy Simulation Model

Acknowledgments
This work was funded by the German Research Foundation (DFG) under Grant RA 617/31-1. All simulations were performed on the Cray XC40 and Atos system of the North-German Supercomputing Alliance (HLRN-3/4) located in Berlin and Göttingen. The LES model PALM is freely available (revision 3094, http://palm.muk.uni-hannover.de/trac/browser/?rev=3094). The output, which was used to generate figures and tables, is accessible via the https://doi.org/10.25835/0095133 website. Also, the user-specific code for detecting dust devils, model steering files, and scripts for postprocessing the raw data is stored there.

References

Alekseenko, S. V., Kuibin, P. A., & Okulov, V. L. (2007). *Theory of concentrated vortices: An introduction*. Heidelberg, HD: Springer. https://doi.org/10.1007/978-3-540-73376-8

Avissar, R., & Schmidt, T. (1998). An evaluation of the scale at which ground–surface heat flux patchiness affects the convective boundary layer using large–eddy simulations. *Journal of the Atmospheric Sciences*, *55*, 2666–2689. https://doi.org/10.1175/1520-0469(1998)055<2666:AEOTSA>2.0.CO;2

Balme, M., & Greeley, R. (1998). Dust devils on Earth and Mars. *Reviews of Geophysics*, *44*, RG3003. https://doi.org/10.1029/2005RG000188

Balme, M., Metzger, S., Towner, M., Ringrose, T., Greeley, R., & Iversen, J. (2003). Friction wind speeds in dust devils: A field study. *Geophysical Research Letters*, *30*(16), 1830. https://doi.org/10.1029/2003GL017493

Bluestein, H. B., Weiss, C. C., & Pazmany, A. L. (2004). Doppler radar observations of dust devils in Texas. *Monthly Weather Review*, *44*, 209–224. https://doi.org/10.1175/1520-0493(2004)132<0209:DROODD>2.0.CO;2

Cellier, P., Richard, G., & Robin, P. (1996). Partition of sensible heat fluxes into bare soil and the atmosphere. *Agricultural and Forest Meteorology*, *82*, 245–265. https://doi.org/10.1016/0168-1923(95)02328-3

Cortese, T., & Balachandar, S. (1993). Vortical nature of thermal plumes in turbulent convection. *Physics of Fluids*, *5*, 3226–3232. https://doi.org/10.1063/1.858679

Deardorff, J. W. (1980). Stratocumulus-capped mixed layers derived from a three-dimensional model. *Boundary-Layer Meteorology*, *18*, 495–527. https://doi.org/10.1007/BF00119502

du Puits, R., Resagk, C., & Thess, A. (2013). Thermal boundary layers in turbulent Rayleigh-Bénard convection at aspect ratios between 1 and 9. *New Journal of Physics*, *15*, 013040. https://doi.org/10.1088/1367-2630/15/1/01304

Durran, D. R. (2010). *Numerical methods for fluid dynamics: With applications to geophysics*. New York, NY: Springer. https://doi.org/10.1007/978-1-4419-6412-0

Gheynani, B. T., & Taylor, P. A. (2010). Large–eddy simulations of vertical vortex formation in the terrestrial and martian convective boundary layers. *Boundary-Layer Meteorology*, *137*, 223–235. https://doi.org/10.1007/s11214-016-0284-x

Gu, Z., Qiu, J., Zhao, Y., & Li, Y. (2008). Simulation of terrestrial dust devil patterns. *Advances in Atmospheric Sciences*, *25*, 31–42. https://doi.org/10.1007/s00376-008-0031-7

Hirsch, C. (2007). *Numerical computation of internal and external flows: The fundamentals of computational fluid dynamics*. Oxford, OXF: Butterworth Heinemann.

Ito, J., Niino, H., & Nakanishi, M. (2013). Formation mechanism of dust devil–like vortices in idealized convective mixed layers. *Journal of the Atmospheric Sciences*, *70*, 1173–1186. https://doi.org/10.1175/JAS-D-12-085.1

Jemmett-Smith, B. C., Marsham, J. H., Knippertz, P., & Gilkeson, C. A. (2015). Quantifying global dust devil occurrence from meteorological analyses. *Geophysical Research Letters*, *42*, 1275–1282. https://doi.org/10.1002/2015GL063078

Kanak, K. M. (2005). Numerical simulation of dust devil–scale vortices. *Quarterly Journal of the Royal Meteorological Society*, *131*, 1271–1292. https://doi.org/10.1256/qj.03.172

Kanak, K. M. (2006). On the numerical simulation of dust devil–like vortices in terrestrial and martian convective boundary layers. *Geophysical Research Letters*, *33*, L19S05. https://doi.org/10.1029/2006GL026207

Kanak, K. M., Lilly, D. K., & Snow, J. T. (2000). The formation of vertical vortices in the convective boundary layer. *Quarterly Journal of the Royal Meteorological Society*, *126*, 2789–2810. https://doi.org/10.1002/qj.49712656910

Koch, J., & Renno, N. O. (2005). The role of convective plumes and vortices on the global aerosol budget. *Geophysical Research Letters*, *32*, L18806. https://doi.org/10.1029/2005GL023420

Letzel, M. O., & Raasch, S. (2003). Large eddy simulation of thermally induced oscillations in the convective boundary layer. *Journal of the Atmospheric Sciences*, *60*, 2328–2341. https://doi.org/10.1175/1520-0469(2003)060<2328:LESOTI>2.0.CO;2

Lorenz, R. D. (2014). Vortex encounter rates with fixed barometer stations: Comparison with visual dust devil counts and large-eddy simulations. *Journal of the Atmospheric Sciences*, *71*, 4461–4472. https://doi.org/10.1175/JAS-D-14-0138.1

Lorenz, R. D. (2016). Heuristic estimation of dust devil vortex parameters and trajectories from single-station meteorological observations: Application to insight at mars. *Icarus*, *271*, 326–337. https://doi.org/10.1016/j.icarus.2016.02.001

Lorenz, R. D., & Jackson, B. K. (2016). Dust devil populations and statistics. *Space Science Reviews*, *203*, 277–297. https://doi.org/10.1007/s11214-016-0277-9

Maronga, B., Gryschka, M., Heinze, R., Hoffmann, F., Kanani-Sühring, F., Keck, M., et al. (2015). The Parallelized Large-Eddy Simulation Model (PALM) version 4.0 for atmospheric and oceanic flows: Model formulation, recent developments, and future perspectives. *Geoscientific Model Development*, *8*, 2515–2551. https://doi.org/10.5194/gmd-8-2515-2015

Metzger, S. M., Balme, M. R., Towner, M. C., Bos, B. J., Ringrose, T. J., & Patel, M. R. (2011). In situ measurements of particle load and transport in dust devils. *Icarus*, *214*, 766–772. https://doi.org/10.1016/j.icarus.2011.03.013

Moeng, C.-H., & Wyngaard, J. C. (1988). Spectral analysis of large-eddy simulations of the convective boundary layer. *Journal of the Atmospheric Sciences*, *45*, 3573–3587. https://doi.org/10.1175/1520-0469(1988)045<3573:SAOLES>2.0.CO;2

Nishizawa, S., Odaka, M., Takahashi, Y. O., Sugiyama, K., Nakajima, K., Ishiwatari, M., et al. (2016). Martian dust devil statistics from high-resolution large-eddy simulations. *Geophysical Research Letters*, *43*, 4180–4188. https://doi.org/10.1002/2016GL068896

Ohno, H., & Takemi, T. (2010). Mechanisms for intensification and maintenance of numerically simulated dust devils. *Atmospheric Science Letters*, *11*, 27–32. https://doi.org/10.1002/asl.249

Parlow, E. (2003). The urban heat budget derived from satellite data. *Geographica Helvetica*, *58*, 99–111.

Patrinos, A. A. N., & Kistler, A. L. (1977). A numerical study of the Chicago lake breeze. *Boundary-Layer Meteorology*, *12*, 93–123. https://doi.org/10.1007/BF00116400

Piacsek, S. A., & Williams, G. P. (1970). Conservation properties of convection difference schemes. *Journal of Computational Physics*, *6*, 392–405. https://doi.org/10.1016/0021-9991(70)90038-0

Raasch, S., & Franke, T. (2011). Structure and formation of dust devil–like vortices in the atmospheric boundary layer: A high–resolution numerical study. *Journal of Geophysical Research*, *116*, D16120. https://doi.org/10.1029/2011JD016010

Rafkin, S., Jemmett-Smith, B., Fenton, L., Lorenz, R., Takemi, T., Ito, J., & Tyler, D. (2016). Dust devil formation. *Space Science Reviews*, *203*, 183–207. https://doi.org/10.1007/s11214-016-0307-7

Renno, N. O., Abreu, V. J., & Koch, J. (2004). Matador 2002: A pilot field experiment on convective plumes and dust devils. *Journal of Geophysical Research*, *109*, E07001. https://doi.org/10.1029/2003JE002219

Renno, N. O., Burkett, M. L., & Larkin, M. P. (1998). A simple thermo-dynamical theory for dust devils. *Journal of the Atmospheric Sciences*, *55*, 3244–3252. https://doi.org/10.1175/1520-0469(1998)055<3244:ASTTFD>2.0.CO;2

Renno, N. O., & Ingersoll, A. P. (1996). Natural convection as a heat engine: A theory for CAPE. *Journal of the Atmospheric Sciences*, *53*, 572–585. https://doi.org/10.1175/1520-0469(1996)053<0572:NCAAHE>2.0.CO;2

Renno, N. O., Nash, A. A., Lunine, J., & Murphy, J. (2000). Martian and terrestrial dust devils: Test of a scaling theory using pathfinder data. *Journal of Geophysical Research*, *105*, 1859–1865. https://doi.org/10.1029/1999JE001037

Sagaut, P. (2006). *Large eddy simulation for incompressible flows: An introduction*. Berlin, BE: Springer. https://doi.org/10.1007/b137536

Saiki, E. M., Moeng, C.-H., & Sullivan, P. P. (2000). Large-eddy simulation of the stably stratified planetary boundary layer. *Boundary-Layer Meteorology*, *95*, 1–30. https://doi.org/10.1023/A:1002428223156

Schmidt, H., & Schumann, U. (1989). Coherent structure of the convective boundary layer derived from large-eddy simulations. *Journal of Fluid Mechanics*, *200*, 511–562. https://doi.org/10.1017/S0022112089000753

Shao, Y., Wyrwoll, K.-H., Chappell, A., Huang, J., Lin, Z., McTainsh, G. H., et al. (2011). Dust cycle: An emerging core theme in Earth system science. *Aeolian Research*, *2*, 181–204. https://doi.org/10.1016/j.aeolia.2011.02.001

Shen, S., & Leclerc, M. Y. (1995). How large must surface inhomogeneities be before they influence the convective boundary layer structure? A case study. *Quarterly Journal of the Royal Meteorological Society*, *121*, 1209–1228. https://doi.org/10.1002/qj.49712152603

Sinclair, P. C. (1969). General characteristics of dust devils. *Journal of Applied Meteorology and Climatology*, *8*, 32–45. https://doi.org/10.1175/1520-0450(1969)008<0032:GCODD>2.0.CO;2

Sinclair, P. C. (1973). The lower structure of dust devils. *Journal of the Atmospheric Sciences*, *30*, 1599–1619. https://doi.org/10.1175/1520-0469(1973)030<1599:TLSODD>2.0.CO;2

Tratt, D. M., Hecht, M. H., Catling, D. C., Samulon, E. C., & Smith, P. H. (2003). In situ measurement of dust devil dynamics: Toward a strategy for Mars. *Journal of Geophysical Research*, *108*(E11), 5116. https://doi.org/10.1029/2003JE002161

Wicker, L. J., & Skamarock, W. C. (2002). Time–splitting methods for elastic models using forward time schemes. *Monthly Weather Review*, *130*, 2088–2097. https://doi.org/10.1175/1520-0493(2002)130<2088:TSMFEM>2.0.CO;2

Williamson, J. H. (1980). Low-storage Runge-Kutta schemes. *Journal of Computational Physics*, *35*, 48–56. https://doi.org/10.1016/0021-9991(80)90033-9